International Journal of Bioprinting

RESEARCH ARTICLE

Synthesis of biocompatible BSA-GMA and two-photon polymerization of 3D hydrogels with free radical type I photoinitiator

Teng Li[1,3], Jie Liu[1], Min Guo[1,3], Fan-Chun Bin[1,3], Jian-Yu Wang[1,3], Atsushi Nakayama[2], Wei-Cai Zhang[1,3], Feng Jin[1], Xian-Zi Dong[1], Katsumasa Fujita[2], Mei-Ling Zheng*[1]

[1]Laboratory of Organic NanoPhotonics and CAS Key Laboratory of Bio-Inspired Materials and Interfacial Science, Technical Institute of Physics and Chemistry, Chinese Academy of Sciences, No. 29 Zhongguancun East Road, Beijing 100190, P. R. China

[2]Department of Applied Physics, Osaka University, 2-1 Yamadaoka, Suita, Osaka 565-0871, Japan

[3]School of Future Technologies, University of Chinese Academy of Sciences, Yanqihu Campus, Beijing 101407, P. R. China

This article belongs to the *Special Issue: Fine-tuned Hydrogels for 3D Bioprinting*)

Abstract

Although the development of three-dimensional (3D) printing technology is growing rapidly in the biomedical field, it remains a challenge to achieve arbitrary 3D structures with high resolution and high efficiency. Protein hydrogels fabricated by two-photon polymerization (TPP) have excellent mechanical properties, high precision, and 3D architecture. However, a large number of the amino acid group in bovine serum albumin (BSA) would be consumed when the protein-based hydrogels use dyes of free radical type II photoinitiators. In this study, we use glycidyl methacrylate (GMA) to modify BSA molecules to obtain a series of BSA-GMA materials, allowing the protein material to be two-photon polymerized with a water-soluble free radical type I photoinitiator. The precisely controllable 3D structure of the BSA-GMA hydrogel was fabricated by adjusting the concentration of the precursor solution, the degree of methacrylation, and the processing parameters of the TPP technique. Importantly, BSA-GMA materials are free of acidic hazardous substances. Meanwhile, the water-soluble initiator lithium phenyl (2,4,6-trimethylbenzoyl) phosphite (LAP) allows TPP on the vinyl group of the GMA chain and thus without consuming its amino acid group. The as-prepared BSA-GMA hydrogel structure exhibits excellent autofluorescence imaging, pH responsiveness, and biocompatibility, which would provide new avenues for potential applications in tissue engineering and biomedical fields to meet specific biological requirements.

Keywords: Two-photon polymerization; Bovine serum albumin; Hydrogel; Free radical type I initiator; Biocompatible scaffold

***Corresponding author:**
Mei-Ling Zheng
(zhengmeiling@mail.ipc.ac.cn)

Citation: Li T, Liu J, Guo M, *et al*., 2023, Synthesis of biocompatible BSA-GMA and two-photon polymerization of 3D hydrogels with free radical type I photoinitiator. *Int J Bioprint,* 9(5): 752. https://doi.org/10.18063/ijb.752

Received: December 30, 2022
Accepted: March 21, 2023
Published Online: May 12, 2023

1. Introduction

The rapid development of three-dimensional (3D) printing technology has attracted increasing attention in the field of tissue engineering[1-4]. The optical crosslinking

system and the optimized functional biomaterials are crucial for light-based 3D printing. To better meet the different needs of scale and precision of synthetic 3D scaffolds, various microfabrication techniques have been developed to construct 3D hydrogels, such as stereolithography[5], soft lithography[6,7], digital light projection[8], electrospinning[9,10], and bioprinting[11,12]. However, it is still a challenge to prepare arbitrarily shaped 3D structures with high resolution and high efficiency. Two-photon polymerization (TPP) as a femtosecond laser direct writing technique allows the rapid polymerization of transparent polymer solutions into arbitrary, high-resolution 3D microstructures, which has been widely used in micro and nano photonics[13,14], microfluidics[15], tissue engineering[16-18], and drug delivery[19,20].

Hydrogel, a kind of advanced material that mimics the extracellular matrix (ECM) *in vivo*, has been extensively investigated for biomedical applications due to its hydrophilicity and potential biocompatibility[21-25]. In the study of hydrogel scaffold materials, natural polymeric materials (collagen[26,27], sodium alginate [SA][28], chitosan[29], hyaluronic acid[30], bovine serum albumin [BSA], etc.) have attracted much attention due to their higher biocompatibility, better flexibility, low toxicity, and greater biodegradability compared to polymeric hydrogels[31-33]. Among them, BSA is a monomeric protein with 583 amino acids and a molecular weight of about 66 kDa, which is highly abundant in plasma at a concentration of about 30–50 mg mL^{-1} and is a non-synthetic and easily available biocompatible material. Furthermore, BSA is a promising scaffold for tissue engineering, regenerative medicine, and drug delivery systems because of its stability, responsiveness to pH and temperature, and ability to gel at low concentrations[34-36]. Albumin-based biomaterials can control the delivery of therapeutic drugs and act as functional biological scaffolds in drug delivery applications[36,37]. Albumin is also used to treat blood loss, burns, and shock due to its clinically established biocompatibility profile for therapeutic applications[38,39]. Numerous studies have demonstrated that negatively charged groups such as carboxyl, hydroxyl, and sulfonic acid groups on the surface of BSA can induce the chondrogenic differentiation of bone marrow mesenchymal stem cells (BMSCs), and promote the adhesion of chondrocytes on the pore surface and the formation of new cartilage[40-42].

However, most protein hydrogels are usually not strong enough to be used as scaffolds because the structure of the protein is mainly maintained by primary-level amide bonds and higher-level non-covalent bonds. Therefore, methods including thermal gelation[43], glutaraldehyde[44], or disulfide bond crosslinking[40] have been reported to modify BSA. However, hydrogels prepared by thermal gelation have poor mechanical properties and are readily soluble in biological fluids. The chemical crosslinking techniques have significant drawbacks in preparing biomaterials with tailored mechanical properties to match different medical applications. Two-photon polymerized protein hydrogels are widely used for tissue engineering and drug delivery because of their excellent mechanical properties and precisely controlled morphology[18,20,45]. TPP usually requires the use of photoinitiators to induce the crosslinking of proteins, which are classified as free radical type I and free radical type II initiators[46-49]. The crosslinking of dye molecules (free radical type II initiators) with proteins involves two photooxidation mechanisms. The first one is to excite the dye molecule to extract hydrogen from the protein molecule to induce protein crosslinking. This mechanism facilitates the crosslinking of proteins containing ketones, phenols, amines, or hydroquinones amino acid residues. The second is that the singlet oxygen continues to react with oxidizable amino acid residues to produce an electron-deficient protein that may react with an amino acid residue of another protein to form a covalent bond[50]. Protein crosslinking is usually favored for tryptophan, tyrosine, or histidine residues as well as amino acid residues containing olefins, diolefins, aromatics, and heterocyclic groups. Therefore, pure BSA can be two-photon polymerized using a type II photoinitiator like Bengal Red, but it consumes a large amount of amino acid groups on BSA[51].

In this study, a series of BSA molecules modified by glycidyl methacrylate (GMA) were synthesized by grafting methacrylate groups to the amine-containing side groups of BSA, which enables the TPP capability using free radical type I photoinitiators. Generally, GMA opens the ring via an epoxide mechanism, and the reaction is stable without acidic by-products. The BSA modified by GMA (BSA-GMA) can interact with free radical type I initiators other than dyes to crosslink without consuming amino acid groups, and the TPP ability of BSA-GMA hydrogels can also be tailored by changing the degree and location of methacrylation. We have evaluated the degree of methacrylation on BSA modified by various amounts of GMA, as well as the TPP performance and 3D printing capabilities of BSA-GMA with different concentrations and degrees of methacrylation. Furthermore, we have demonstrated that the as-prepared BSA-GMA hydrogels have autofluorescence, pH-responsive characteristics, and good biocompatibility. The proposed synthesis strategy and the protocol for TPP of 3D bioinspired microstructures would provide

Table 1. BSA and GMA ratios for modification experiments

n_{lysine}/n_{GMA}	m_{BSA} (g)	n_{lysine} (mmol)	n_{GMA} (mmol)	V_{GMA} (μL)	Methacrylation degree (%)
1:1	5	4.45	4.45	577.5	15
1:1.5	5	4.45	6.68	865	35
1:2	5	4.45	8.90	1155	52

guidance to the development of functional materials for tissue engineering and biomedical fields.

2. Materials and methods

2.1. Materials

BSA, Hoechst 33342, dialysis membrane, and TESCA buffer (50 mM TES [$C_6H_{15}NO_6S$], 0.36 mM $CaCl_2$, pH 7.4) were purchased from Solarbio (Beijing, China). GMA and rose bengal (RB) were acquired from Sigma Aldrich (St. Louis, Missouri, MO, USA). Phosphate-buffered solution (PBS; pH = 7.4) was purchased from Leagene Biotechnology Co., Ltd, (Beijing, China). Rabbit articular chondrocytes and rabbit articular chondrocytes complete culture medium were acquired from Procell Life Science&Technology Co., Ltd (Wuhan, China). Mito-Tracker Deep Red and propidium iodide (PI) were purchased from Invitrogen, Ltd. (UK). LAP was acquired from TCI Development Co., Ltd (Shanghai, China).

2.2. Synthesis of BSA-GMA

BSA (5 g) was dissolved in 25 mL PBS and stirred for half an hour at room temperature until completely dissolved. The mature BSA protein with a molecular weight of about 66.5 kDa contains 583 amino acids, of which 59 are lysines according to the manual for BSA.

$$n_{lysine} = (m_{BSA} \times 59)/M_{BSA} \quad (I)$$

As shown in Table 1, BSA-GMA was synthesized by adding 577.5, 865, and 1155 μL of GMA solution dropwise to the BSA solution, and the reaction was carried out at room temperature for 5 days. The solution was diluted five-fold with PBS and stirred for 30 min to terminate the reaction. The solution was dialyzed with deionized water for 5 days using a 12–14 kDa cut-off dialysis membrane. Finally, the methacrylated BSA solution was freeze-dried. The freeze-dried BSA-GMA powders were stored at -20°C for further use.

2.3. Molecule structure characterization by ^{1}H-NMR/FT-IR

The powders of BSA and BSA-GMA synthesized with different lysine/GMA molar ratios of 1:1, 1:1.5, and 1:2 were measured by Fourier transform infrared spectrometer (FT-IR) to evaluate the graft of GMA onto BSA. The samples for FT-IR characterization were prepared by grinding the powders with potassium bromide (KBr), while GMA was coated on the surface of the KBr slice. Proton nuclear magnetic resonance (^{1}H-NMR) characterization was used to further determine the degree of methacrylation by a Bruker DPX FT-NMR spectrometer (9.4 T) at 400 MHz. BSA (50 mg) and each BSA-GMA were dissolved in 550 μL Deuterium oxide (D_2O) and characterized by ^{1}H-NMR, respectively. The degree of methacrylation was defined by the percentage of the signal of the methacrylate group at δ = 5.7 and δ = 6.1 ppm versus the proton signal generated by the aromatic amino acids at 6.6–7.4 ppm in BSA-GMA.

$$\%\text{Degree of methacrylation} = (A_{\delta=5.7} + A_{\delta=6.1})/A_{\delta=7.0} \times 100 \quad (II)$$

Table 2. Main components of the as-prepared photoresist precursors

Sample	BSA-GMA (mg, wt%)	LAP (mg, wt%)	H_2O (μL)
$R_{20}D_{52}$	125.8 (20 wt%)	3.14 (0.5 wt%)	500
$R_{30}D_{52}$	214.3 (30 wt%)	3.62 (0.5 wt%)	500
$R_{40}D_{52}$	336.2 (40 wt%)	4.2 (0.5 wt%)	500
$R_{40}D_{35}$	336.2 (40 wt%)	4.2 (0.5 wt%)	500
$R_{40}D_{15}$	336.2 (40 wt%)	4.2 (0.5 wt%)	500

2.4. Preparation of hydrogel precursor solution

First, freeze-dried BSA-GMA powder with 52% methacrylation degree and 0.5 wt% photoinitiator LAP were dissolved in ultrapure water to form precursor solutions of 20 wt% BSA-GMA (52%), 30 wt% BSA-GMA (52%), and 40 wt% BSA-GMA (52%). Then, the BSA-GMA powders with 15% and 35% methacrylation degree and 0.5 wt% of photoinitiator LAP were added in ultrapure water to form 40 wt% BSA-GMA (15%) and 40 wt% BSA-GMA (35%) precursor solutions. Table 2 shows the main components of the as-prepared photoresist precursors. The hydrogels are defined by the weight ratio (R) and degree of methacrylation (D) and abbreviated as $R_{20}D_{52}$, $R_{30}D_{52}$, $R_{40}D_{52}$, $R_{40}D_{15}$, and $R_{40}D_{35}$, respectively. The precursor solutions were fully stirred in a dark room and stored in a refrigerator at 4°C.

2.5. TPP microfabrication of BSA-GMA hydrogels

In the fabrication experiment, a home-built laser direct writing optical setup was used to fabricate 3D microstructures of BSA-GMA hydrogels (**Figure S1** in Supplementary File). A near-infrared Ti: sapphire femtosecond laser beam with a central wavelength of 780 nm, a pulse width of 80 fs, and a repetition rate of 80 MHz was used. The laser beam was tightly focused into the photoresist by an oil immersion objective lens (60×, numerical aperture 1.42, Olympus). Before the fabrication

processing, the BSA-GMA precursor solution was dropped between two coverslips placed on an *XYZ* positioning stage. The photoresist was scanned by a femtosecond laser beam in 3D by a computer-controlled *XYZ* motorized stage (Physik Instrumente). After the fabrication, the unpolymerized BSA-GMA solution was washed with deionized water, and the desired 3D microstructure can be achieved. Scanning electron microscope (SEM) images were characterized by a field emission scanning electron microscope (FESEM, Hitachi S-4800). Confocal fluorescence images were recorded by a laser scanning confocal fluorescence microscope (A1 MP, Nikon).

2.6. Optical characterization of precursors and microstructures of BSA and BSA-GMA

UV-Vis absorption spectra were characterized by a Shimadzu UV-2550 spectrophotometer. The concentration of initiator in the initiator solution was 8.55×10^{-3} g mL^{-1}. The BSA-GMA aqueous solution was prepared from BSA-GMA powder with 52% degree of methacrylation and 40 wt% concentration without initiator as a control, as well as the solutions of $R_{20}D_{52}$, $R_{30}D_{52}$, $R_{40}D_{15}$, $R_{40}D_{35}$, and $R_{40}D_{52}$ containing 0.5 wt% initiators. Infrared spectra of GMA, precursor solution, and microstructure of BSA+RB, as well as precursor solution and microstructure of BSA-GMA were performed with a Fourier transform infrared micro-spectrometer (Vertex 70 Micro and Hyperion 1000-2000) in the range of 600 to 4000 cm^{-1}. Raman spectra and images were measured by a Raman-11 microscopy using a 532-nm laser as the excitation source in line scanning mode.

2.7. Zeta potential and isoelectric point of BSA and BSA-GMA with different methacrylation degrees

The electrical properties were characterized using a Zetasizer (Nano ZS90, Malvern, UK) under different pH conditions. Sodium phosphate dibasic-Citric acid (Na_2HPO_4-CA) buffer solutions were prepared at pH 2.66, 3.15, 3.45, 3.79, 4.07, 4.52, 4.96, 5.22, 6.09, 6.97, and 8.16, respectively. BSA and BSA-GMA were dissolved in Na_2HPO_4-CA buffer solutions at different pH values at a concentration of 10 μg mL^{-1}, and the zeta potential values of various samples were measured. The isoelectric point is the pH value at a zeta potential of 0 mV. The isoelectric point of the material is obtained by a linear fitting to two pH values across 0 mV.

2.8. pH response experiment

First, $7 \times 7 \times 2$ μm^3 sized hydrogel cubes were polymerized by the TPP technique. Afterward, 200 μL of different pH solutions were dropped onto coverslips containing the hydrogel structures at room temperature, and the pH response process was recorded under a microscope with a CCD DS-Ri2 (Nikon, Japan) and a 50× objective lens (N.A. = 0.8). pH response experiments were performed with pH 2, pH 5, PBS (pH 7.4), and pH 11 solutions, in which the solutions of different pH were prepared with concentrated HCl and NaOH.

2.9. Evaluation of cell viability in BSA-GMA hydrogels

3D microscaffolds of $R_{20}D_{52}$, $R_{30}D_{52}$, $R_{40}D_{52}$, $R_{40}D_{35}$, and $R_{40}D_{15}$ were prepared in each coverslip by the TPP technique. Before cell culture, the cell scaffolds were sterilized with 75% ethanol and ultraviolet (UV) light for 1 h, respectively. Rabbit articular chondrocytes were cocultured with five cell scaffolds using chondrocyte-specific medium, and incubated in a humidified incubator at 37°C and 5% CO_2 for 72 h. The medium was changed every other day. The mitochondria of living cells were stained with Mito-Tracker Deep Red for 20 min, and then, the nuclei of living cells were stained with Hoechst 33342 for 10 min. Dead cell nuclei were then stained with PI for 10 min. The fluorescence images were observed using confocal fluorescence microscope with a 20× objective lens. The excitation wavelengths were 640, 561, 488, and 405 nm, respectively.

3. Results and discussion

In this work, GMA was used to modify BSA to obtain a series of BSA-GMA materials, which can not only be two-photon polymerized using water-soluble radical type I photoinitiators without depleting the amino acid groups of the protein, but can also be adjusted according to the degree of methacrylation to tune the TPP capability. Moreover, the polymerized BSA-GMA hydrogel structure exhibited autofluorescence, pH response, and excellent biocompatibility.

3.1. BSA-GMA preparation and characterization

BSA has low toxicity, high biocompatibility, and good flexibility, and can be easily polymerized into hydrogels, showing a wide range of applications in various fields. BSA consumes a large number of amino acid residues via TPP based on a dye-amine system. Many of these amino acid residues are important for cells, which are essential for cell attachment to protein scaffolds. Thus, we modified BSA by GMA so that the TPP reaction only occurs at the double bond on the GMA chain without consuming amino acid groups with type I initiators. This overcomes the limitation of consuming amino acids using free radical type II initiators in TPP of BSA (Figure 1). The BSA-GMA was synthesized by replacing the primary amines of BSA with GMA (Figure 1A). GMA reacts with the primary amine ($-NH_2$) of the lysine residue of BSA via an epoxide ring-opening mechanism without acidic by-products[52]. GMA

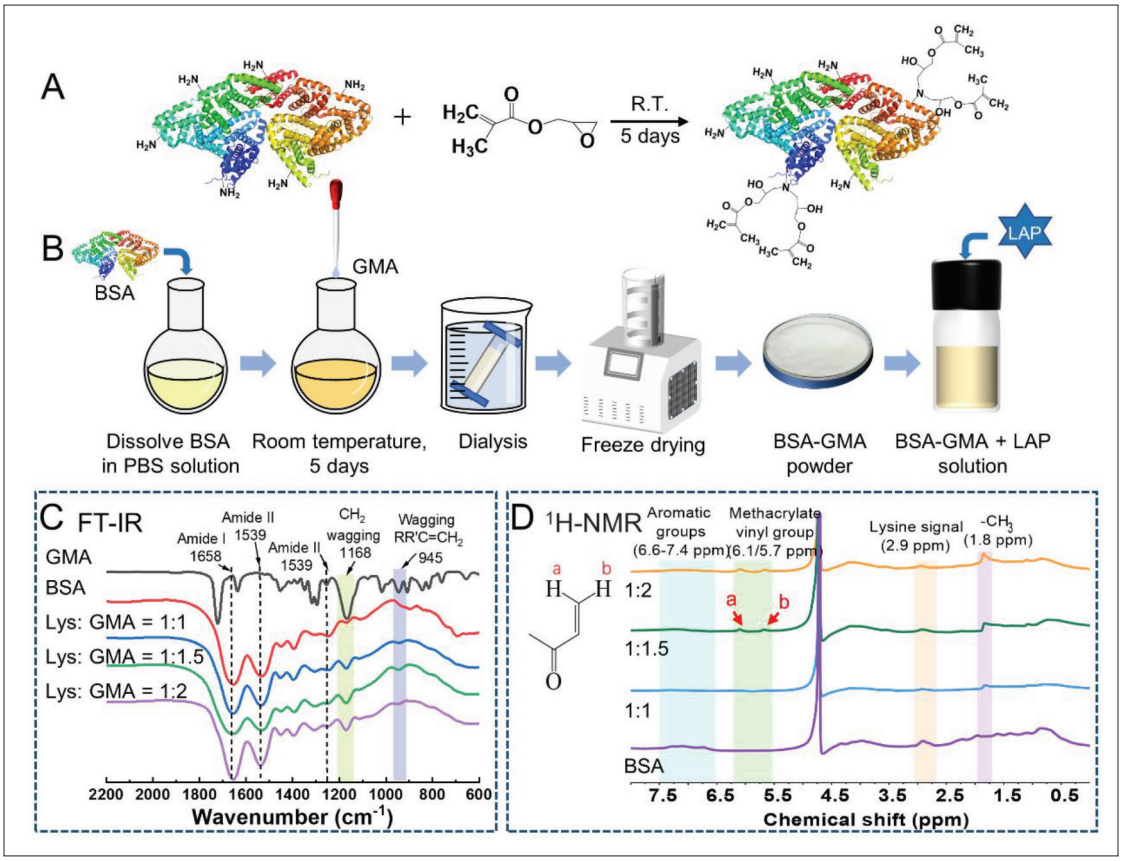

Figure 1. BSA-GMA as pre-hydrogel as well as FT-IR spectra and ^{1}H-NMR spectra of unsubstituted BSA and BSA-GMA with different degrees of methacrylation. (A) Modification of BSA with GMA. BSA is covalently immobilized with GMA, which is a donor of the vinyl double bond as a two-photon crosslinking site. (B) BSA powder was dissolved in PBS at pH 7.4, and GMA was added dropwise to this solution after half an hour and reacted at room temperature for 5 days. It was dialyzed in distilled water for 3 days to remove the salt and then freeze-dried. A precursor solution was prepared by adding LAP to the BSA-GMA solution. (C) FT-IR spectra of GMA, unsubstituted BSA, and BSA-GMA with different degrees of methylation. In FT-IR spectra, amide I (1639 cm^{-1}), amide II (1512 cm^{-1}), and amide III (1234 cm^{-1}) in BSA were found, as well as spectra related to GMA, such as at 951 and 1165 cm^{-1}, -CH_2 wagging stretching of methacrylate vinyl. (D) ^{1}H-NMR spectra of unsubstituted BSA and BSA-GMA with different degrees of methylation. The modification of lysine residues in BSA was confirmed with increasing GMA, with a gradual decrease in lysine signal at δ = 2.9 ppm, an increase in methacrylate vinyl signal at δ = 6.2–5.9 and 5.8–5.5 ppm, and an increase in methyl signal at δ = 1.8 ppm.

can increase the reaction with amino groups, and two GMA molecules can react with one free amino group. GMA can also increase the amount of vinyl methacrylate by reacting with the hydroxyl and carboxyl groups in BSA through an esterification mechanism, thus maximizing the crosslink density of BSA-GMA hydrogels[53]. To optimize the ratio of BSA-GMA hydrogels, BSA-GMA was fabricated by adding GMA with lysine group ratios of 1:1, 1:1.5, and 1:2 into the BSA solution, respectively (Figure 1B). A series of BSA-GMA powders were synthesized by the methacrylation reaction, followed by dialysis and freeze-drying. LAP has good water solubility, good biocompatibility, and a two-photon absorption (TPA) of 0.16 GM at 800 nm, which is promising for TPP initiator[54,55]. Therefore, we chose LAP as the type I initiator for this study.

The modification of GMA on BSA was confirmed by the identification of GMA-related peaks and BSA-related peaks in FT-IR (Figure 1C). BSA-GMA powders were named according to the molar ratio of lysine and GMA in the reaction. The variations of the BSA-GMA peaks were determined by comparing the peaks of pure BSA and GMA. The spectra of pure BSA and all Lys: GMA samples showed protein-related amide I, II, and III peaks at 1658, 1539, and 1246 cm^{-1}, respectively. The IR spectra of GMA showed strong -CH_2 swing and stretching vibrations of vinyl at 1168 and 945 cm^{-1}. The changes detected in the BSA-GMA specimens compared to the BSA were at 1168 and 945 cm^{-1}, representing the -CH_2 wagging stretching of vinyl in GMA. These peaks increase gradually with the increase of the GMA ratios. To further quantify the degree of methacrylation of BSA-GMA under each condition, it was characterized ^{1}H-NMR spectroscopy (Figure 1D). Specifically, the characteristic resonances of methacrylic acid vinyl groups (δ = 6.1 and 5.7 ppm) and GMA methyl (δ = 1.8 ppm) appeared after the addition of

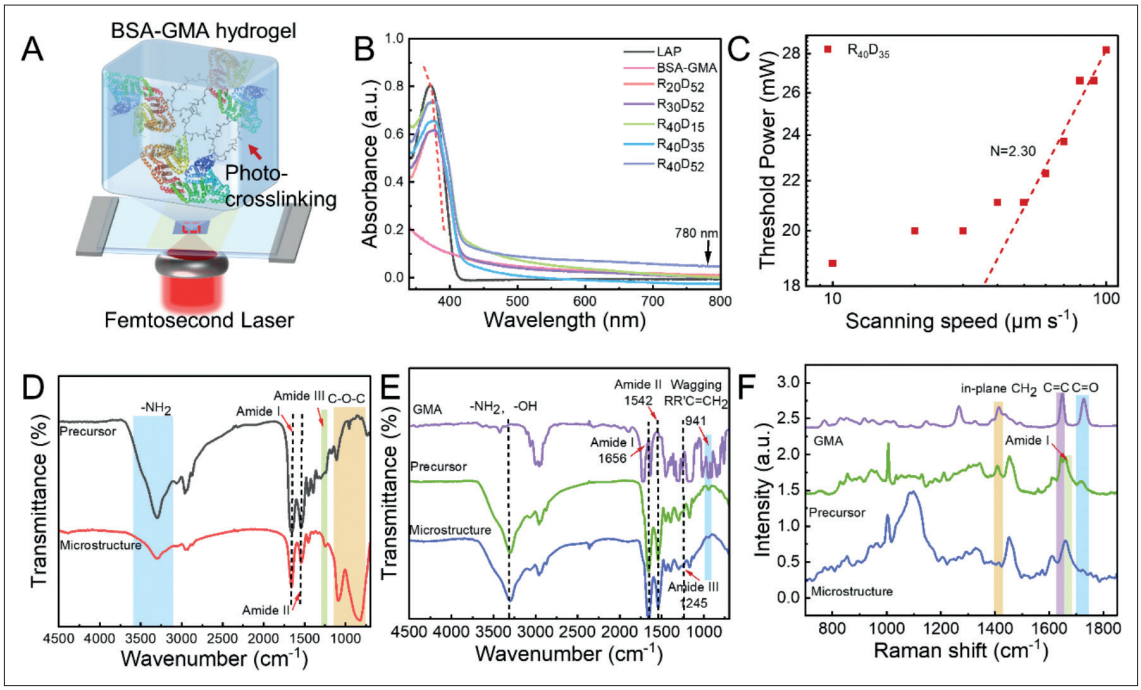

Figure 2. BSA-GMA TPP mechanism. (A) Schematic diagram of BSA-GMA polymerization mechanism. (B) UV-Vis absorption spectra of LAP solution, BSA-GMA solution and BSA-GMA precursor solution. (C) TPP laser threshold power as a function of scanning speed for the photoresist $R_{40}D_{35}$. (D) FT-IR micro-spectroscopy spectra of BSA+RB precursor and microstructure by TPP. (E) FT-IR micro-spectroscopy spectra of $R_{40}D_{52}$ precursor and microstructure by TPP. (F) Raman spectra of $R_{40}D_{52}$ precursor and microstructure by TPP.

GMA, and the integration of these peaks increased with the increase of the amount of GMA. The lysine methylene signal at δ = 2.9 ppm gradually decreased with increasing GMA content, indicating the changes in lysine residues in BSA. The degree of methacrylation was calculated by dividing the area under the double peaks of δ = 5.7 and δ = 6.1 ppm (methacrylate groups) by the area under the peak of δ = 7.0 ppm (aromatic groups)[56]. The degrees of methacrylation for Lys: GMA = 1:1, Lys: GMA = 1:1.5, and Lys: GMA = 1:2 were determined as 15%, 35%, and 52%, respectively (**Figure S2** in Supplementary File). ^{1}H-NMR analysis showed that the degree of methacrylation was the highest for Lys: GMA = 1:2. The amount of methacrylate increased in proportion to the volume of GMA used in the synthesis reaction, while the lysine content decreased with the increasing volume of GMA. It is demonstrated that epoxide ring opening on GMA and nucleophilic addition of lysine depends on the amount of GMA. GMA has been successfully grafted onto BSA as demonstrated by FT-IR and ^{1}H-NMR. The degree of methacrylation in this study is synthesized in the range of 15% to 52%.

3.2. TPP mechanism of BSA-GMA hydrogel

The modified BSA-GMA can be used in TPP with type I photoinitiators other than type II photoinitiators. The TPP mechanism of BSA-GMA was verified by comparing the optical properties of the precursor and microstructure (Figure 2). Figure 2A is a schematic diagram of the hypothesized crosslinking network for the TPP of BSA-GMA hydrogels. The photoinitiator LAP in the BSA-GMA precursor solution absorbed two photons under the femtosecond laser irradiation at 780 nm, which triggered the opening of the double bond of vinyl on GMA for free radical polymerization and formed a polymerization network. The UV absorption spectra of the photoinitiator LAP solution, the aqueous BSA-GMA solution, and the BSA-GMA hydrogel precursor solution were analyzed by UV-Vis absorption spectroscopy (Figure 2B). The absorption peak of the LAP solution was at 370 nm, and the addition of BSA-GMA resulted in a slight red shift of the BSA-GMA precursor solution with the absorption peak at 378 nm, while the pure BSA-GMA solution showed no absorption at 378 nm. All solutions showed no absorption at 780 nm, which demonstrates that the polymerization of BSA-GMA with a type I initiator at 780 nm is not a single-photon polymerization. The laser threshold power of BSA-GMA has a power-law relationship with the scanning speed and can be used to determine the mechanism of the polymerization reaction[57]. When the laser writing speed is below 50 μm s^{-1}, P_{th} is significantly higher than the mathematical fitted value (straight dashed line). It is because the rate of free radical generation in TPP hydrogels

is higher than the rate of oxygen diffusion into the exposed volume, independent of the exposure time and the laser writing speed at the lower laser writing speed[58]. Thus, only the data at high scanning speeds were chosen for the fitting. For the higher scanning speeds ($V_s \geq 50$ μm s^{-1}),

$$P_{th} \propto C \times V_S^{1/N} \quad \text{(III)}$$

where N is the non-linear exponent of the photoinitiator and C is a constant related to the fabrication performance of the photoresist. We investigated the relationship between the laser threshold power and the scanning speed using the $R_{40}D_{35}$ photoresist as an example. The N value obtained from Figure 2C is 2.3, which is close to the two-photon absorption coefficient. The TPP mechanisms of BSA and BSA-GMA were studied by FT-IR micro-spectroscopy and Raman, respectively. Figure 2D shows the FT-IR spectra of the BSA+RB precursor solution and the microstructure by TPP. The broad absorption peak at 3311 cm^{-1} is the characteristic peak of BSA with significantly decreasing peak intensity after polymerization, which is the stretching vibration of the amino (single bond -NH_2) group and the hydroxyl (O-H) group. Amide I, amide II, and amide III show peaks at 1660, 1540, and 1249 cm^{-1}, respectively. The intensity of the peak of amide II decreased and that of amide III increased. Moreover, strong C-O-C peaks have been observed at 831 and 1081 cm^{-1}, which are thought to be the oxidation of some phenolic hydroxyl groups on BSA tyrosine residues by the excited state of RB and coupling with other amino acid residues to form C-O-C bonds. The decrease in the intensity of the amino acid peak and the appearance of the C-O-C peak suggests that the TPP in the BSA+RB system consumes a large number of amino acid residues. These amino acid residues are essential for cell attachment to protein scaffolds, so the depletion of primary amino groups and carboxylate groups can affect the biocompatibility of the scaffold[38,59].

In contrast, TPP of BSA-GMA using a radical I type photoinitiator occurs only on the GMA chain and does not consume amino acid groups. Figure 2E shows the FT-IR micro-spectroscopy spectra of GMA, BSA-GMA precursor solution, and the microstructure by TPP. The broad absorption peak exhibited at 3417 cm^{-1} is the characteristic peak of BSA, which is the stretching vibration of N-H and O-H bonds. Amide I, amide II, and amide III show peaks at 1656, 1542, and 1245 cm^{-1}, respectively. Most of the FT-IR micro-spectroscopy peaks were retained after the TPP, and the characteristic peak wagging C=CH_2 of GMA was at 942 cm^{-1}, which was significantly weakened after polymerization. This result indicates that the C=C bond in BSA-GMA is initiated by a radical type I initiator under a femtosecond laser to achieve TPP. Figure 2F shows the Raman spectral analysis of GMA, $R_{40}D_{52}$ precursor, and microstructure by TPP, which also demonstrates the two-bond opening of vinyl on GMA during two-photon crosslinking. The =CH_2 bending vibration, C=C stretching vibration, and C=O stretching vibration of GMA in Raman spectroscopy were reported as 1425, 1644, and 1732 cm^{-1}, respectively[60,61]. Before the polymerization, BSA-GMA has Raman peaks of 1410 cm^{-1} as an in-plane deformation vibration of =CH_2 on GMA, 1643 cm^{-1} as a C=C double bond stretching with the C=O peak of amide I of BSA forming a double peak, and 1720 cm^{-1} as a C=O vibration peak on the GMA chain. After TPP, most of the Raman peaks were still preserved. However, the Raman intensity of some peaks decreased or disappeared. The Raman intensity at 1409 cm^{-1} (the deformation of =CH_2 in the face) decreased after TPP, and the disappearance of the peak at 1643 cm^{-1} changed from a double peak to a single peak. These results suggest that the C=C bond in BSA-GMA was depleted. The intensity of the C=O peak at 1720 cm^{-1} was also weakened, which was thought to be the disappearance of the C=C double bond leading to the loss of the conjugated system. The analyses of UV-Vis absorption spectra, FT-IR micro-spectroscopy, and Raman spectra demonstrate that the BSA-GMA precursor solution with LAP as photoinitiator under the femtosecond laser at a wavelength of 780 nm is a TPP process, and the site of polymerization is the vinyl group on the GMA chain without consuming other amino acid residues.

3.3 TPP properties of BSA-GMA hydrogels

The hydrogel precursor solution contains the BSA-GMA as the monomer and the LAP as the photoinitiator. Many parameters could affect the quality of BSA-GMA hydrogels, including laser power as well as the degree of methacrylation and the concentration of BSA-GMA. To fabricate highly precise and stable protein microstructures under appropriate conditions, the TPP properties of BSA-GMA precursor solutions with different concentrations and different degrees of methacrylation were first investigated. The fabrication performance of the BSA-GMA hydrogel systems was evaluated by laser threshold power, fabrication resolution, and 3D fabrication capability.

To determine the laser threshold power and the line width of different BSA-GMA hydrogels, the relationship between line width and laser scanning power was investigated at a constant scanning speed of 10 μm s^{-1}. When the scanning speed was set as a constant, the higher the starting efficiency of the photoinitiator, the lower the polymerization threshold. Figure 3 shows the TPP properties of the $R_{20}D_{52}$, $R_{30}D_{52}$, $R_{40}D_{15}$, $R_{40}D_{35}$, and $R_{40}D_{52}$ hydrogel systems, and the TPP laser threshold powers of 13.6, 12.3, 18.0, 13.3, and 5.6 mW, respectively. When the power is below the threshold, the obtained hydrogel line

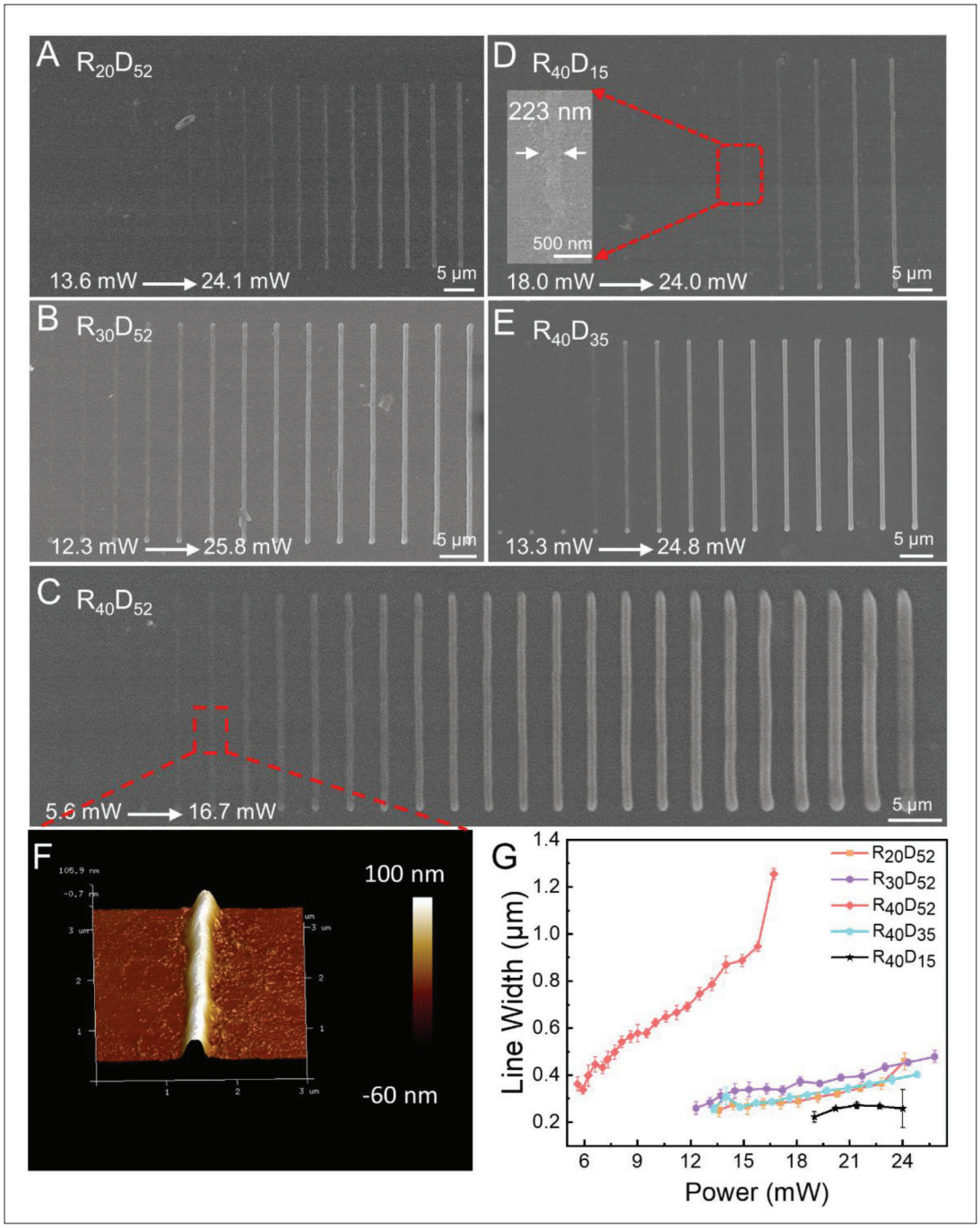

Figure 3. The effect of BSA-GMA concentration, methacrylation degree, and laser power on BSA-GMA polymerization line. SEM images of the polymerization lines of (A) $R_{20}D_{52}$, (B) $R_{30}D_{52}$, (C) $R_{40}D_{52}$, (D) $R_{40}D_{15}$, and (E) $R_{40}D_{35}$. (F) AFM image of $R_{40}D_{52}$ polymerization line. (G) The effect of laser power on the line width of BSA-GMA with different concentrations and degrees of methacrylation.

structures were incomplete. Figure 3A–C shows SEM images of the polymerization lines for different concentrations of BSA-GMA, with the threshold power decreasing from 13.6 to 5.6 mW as the BSA-GMA concentration increases from 20 wt% to 40 wt%. As the degree of methacrylation increased from 15% to 52%, the threshold power decreased from 18 to 5.6 mW (Figure 3C-E). **Figure S3** (Supplementary File) shows the line structure obtained by TPP with 30 wt% BSA as monomer and 0.5 wt% LAP as initiator. The TPP process of the BSA+LAP system only occurs at the laser power range of 20–23.7 mW. The TPP ability of the pure BSA system was poor compared

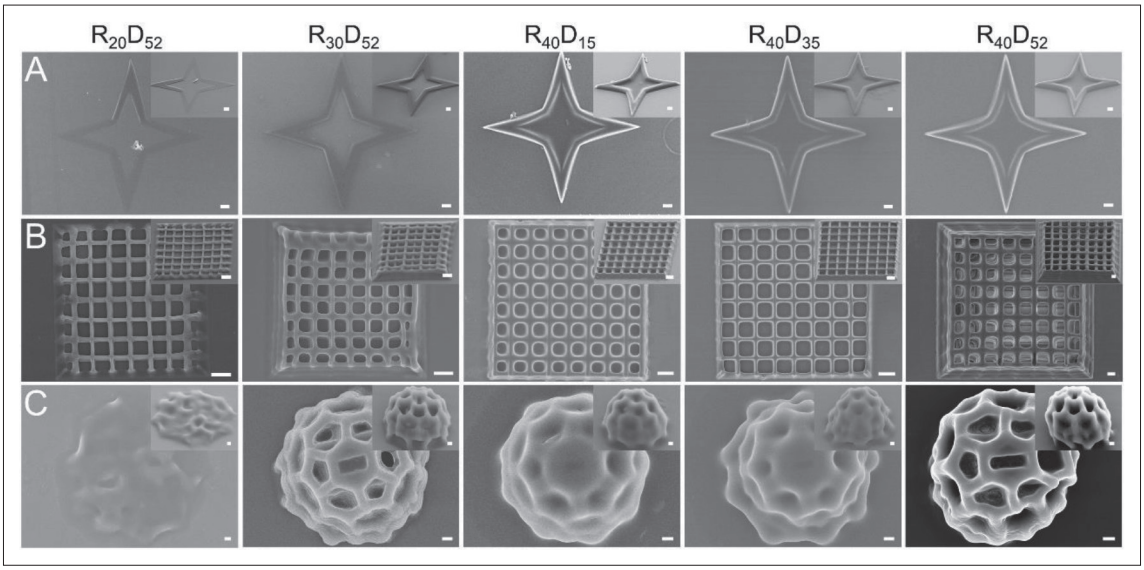

Figure 4. SEM images of arbitrary 3D structures of BSA-GMA hydrogels with different contents and degrees of methacrylation processed by TPP. (A) SEM images of four-pointed star structures of BSA-GMA hydrogels. Scale bar: 5 μm. (B) SEM images of woodpile structures of BSA-GMA hydrogels. Scale bar: 5 μm. (C) SEM images of hollow cage construction of BSA-GMA hydrogels. Scale bar: 1 μm.

Table 3. TPP parameters for 3D structures

Sample	Four-pointed star	Woodpile structures	Hollow cage
$R_{20}D_{52}$	P = 17.2 mW, V = 110 μm/s	P = 15.9 mW, V = 10 μm/s	P = 37.0 mW, V = 22 μm/s
$R_{30}D_{52}$	P = 14.2 mW, V = 110 μm/s	P = 17.7 mW, V = 10 μm/s	P = 11.0 mW, V = 22 μm/s
$R_{40}D_{15}$	P = 8.1 mW, V = 110 μm/s	P = 13.9 mW, V = 50 μm/s	P = 12.9 mW, V = 88 μm/s
$R_{40}D_{35}$	P = 6.1 mW, V = 110 μm/s	P = 13.9 mW, V = 50 μm/s	P = 12.8 mW, V = 22 μm/s
$R_{40}D_{52}$	P = 6.0 mW, V = 110 μm/s	P = 4.3 mW, V = 10 μm/s	P = 5 mW, V = 22 μm/s

to the BSA-GMA system. The minimum resolution of the line width decreases with decreasing concentration and methacrylation degree, from 362 nm for $R_{40}D_{52}$ to 250 nm for $R_{20}D_{52}$ and 199 nm for $R_{40}D_{15}$. Figure 3F shows the atomic force microscopy (AFM) image of the $R_{40}D_{52}$ line structure, and the line height is 107 nm. The data of the BSA-GMA system are summarized in Figure 3G to thoroughly study the relationship between line width and polymerization power. The polymerization threshold power decreases with increasing concentration and degree of methacrylation, and the line width increases linearly with increasing power. The trend is similar for $R_{40}D_{15}$, $R_{40}D_{35}$, $R_{20}D_{52}$, and $R_{30}D_{52}$, while $R_{40}D_{52}$ shows an abrupt change, and the line width varies more with increasing power. BSA-GMA has better TPP ability with free radical type I photoinitiator compared with pure BSA. The TPP characteristics of BSA-GMA can be adjusted according to the degree of methacrylation and the concentration of BSA-GMA, where the degree of methacrylation has a more obvious effect on the TPP.

To get the actual accuracy and 3D microstructure capability of this photoresist system in TPP, the optimal 3D structure of each hydrogel system was obtained by adjusting the processing parameters. We simulated the printing of arbitrary shapes from 2D to complex 3D as an example of a two-photon polymerized BSA-GMA hydrogel (Figure 4). Table 3 shows the laser processing parameters for the fabrication of 3D structures for each hydrogel system. As the concentration and the degree of methacrylation increased, less laser power was required. Figure 4A shows the four-pointed star structures that illustrate the ability of the BSA-GMA hydrogel to process sharp patterns with TPP. The BSA-GMA with concentrations of 20 wt% and 30 wt% used high laser power, but only a shallow height of hydrogel structure was obtained. In contrast, the polymerization power of the three samples with different degrees of methacrylation, $R_{40}D_{15}$, $R_{40}D_{35}$, and $R_{40}D_{52}$, decreased with increasing degrees of methacrylation, and the 3D structures were clear without significant differences. All five BSA-GMA woodpile structures shrunk at a small degree, among which $R_{20}D_{52}$, $R_{40}D_{15}$, and $R_{40}D_{35}$ had low heights without obvious lays (Figure 4B). The woodpile structures of $R_{30}D_{52}$ and $R_{40}D_{52}$

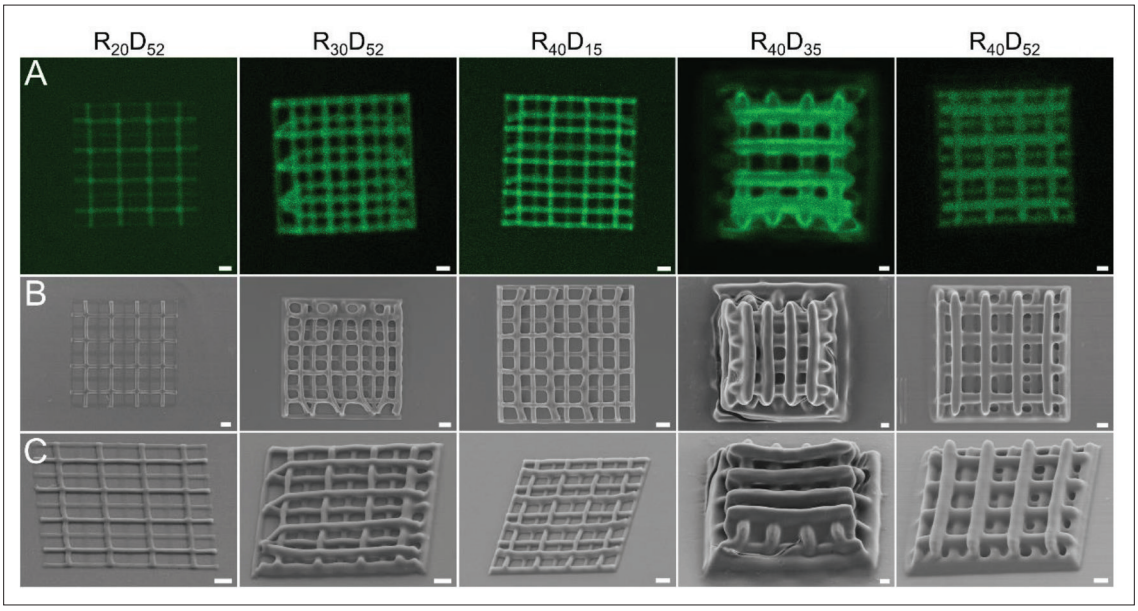

Figure 5. Confocal fluorescence images and SEM images of the autofluorescent BSA-GMA structures. (A) Fluorescence images of five BSA-GMA structures were collected by confocal fluorescence microscopy with a 488 nm laser. Scale bar: 5 μm. (B) SEM images of the BSA-GMA structures. Scale bar: 5 μm. (C) Oblique view of the SEM images of the BSA-GMA structures. Scale bar: 5 μm.

with high concentration and high methacrylation degree had higher heights and clearer layers compared with the first three structures. Figure 4C shows a more complex hollow cage structure. Several photoresist systems except $R_{20}D_{52}$ could maintain 3D structure, but $R_{40}D_{15}$ and $R_{40}D_{35}$ had no hole structure on the surface. The holes of the hollow cage structure of $R_{30}D_{52}$ and $R_{40}D_{52}$ were obvious, among which $R_{40}D_{52}$ had the complete structure, the best simulation, and the least deformability at the smallest polymerization power of 5 mW. These results showed that three types of 3D structures ranging from simple to complex were prepared by TPP: a four-pointed star, a wooden pile, and a hollow cage, with the $R_{40}D_{52}$ system having the best ability to polymerize 3D structures by TPP. The as-prepared hydrogels not only exhibit the TPP fabrication capability, but also enrich the 3D hydrogels with desirable structural configuration.

3.4 Characteristics of BSA-GMA hydrogels

BSA exhibits an intrinsic autofluorescence (excitation/emission at 279 nm/348 nm) attributed to two tryptophan residues. Moreover, the crosslinked BSA hydrogels show fluorescence at the excitation wavelengths of 470 and 595 nm, respectively[62]. We prepared five BSA-GMA hydrogel woodpile structures by femtosecond laser, and the two-photon polymerized BSA-GMA hydrogels exhibited autofluorescence, which could be observed by confocal fluorescence microscopy using 488 nm (Figure 5). As shown in Figure 5A, all five BSA-GMA hydrogels with different concentrations and different degrees of methacrylation exhibited autofluorescence characteristics. Figure 5B and C shows the SEM images and oblique views of SEM images of the five BSA-GMA woodpile structures, respectively. As shown in the oblique view of SEM, the high concentration and high degree of methacrylation of BSA-GMA can create 3D structures with high height demand. The autofluorescence of BSA-GMA hydrogels can play a critical role in drug delivery and tissue engineering.

Proteins have the ability to change shape in response to external pH stimuli due to a large number of carboxylic acid groups and amino groups[63-65]. The electrical properties of BSA and BSA-GMA samples with 15%, 35%, and 52% methacrylation degree (abbreviated as D_{15}, D_{35}, and D_{52}) were measured by zeta potential at different pH values, and the isoelectric points were determined. As shown in Figure 6A, the zeta potential values of both BSA and BSA-GMA samples of D_{15}, D_{35}, and D_{52} gradually decreased with the increase of pH. As BSA is an amphoteric electrolyte, the isoelectric point of BSA is determined by the amino group (basic group) and the carboxyl group (acidic group) on the side chain of amino acid residues. Figure 6B shows the isoelectric points of BSA, D_{15}, D_{35}, and D_{52}. The results show that the isoelectric point of BSA-GMA is slightly higher than that of BSA and increases with the increase of methacrylation degree. Two hydroxyl groups in GMA chain can be grafted on one lysine group, resulting in more negatively charged groups and the consequent increase in the isoelectric point. Moreover, one amino group can bring

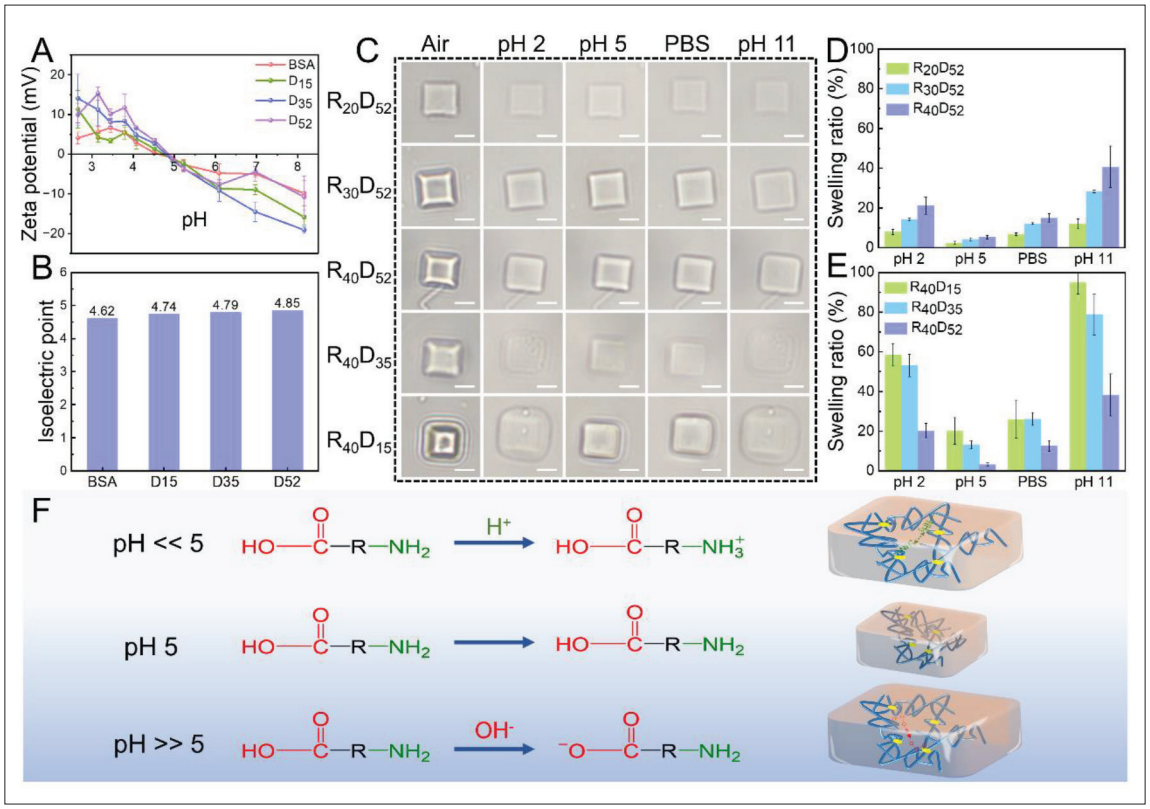

Figure 6. pH-responsive properties of BSA-GMA hydrogel. (A) Zeta potentials of BSA and BSA-GMA with different degrees of methacrylation (D_{15}, D_{35}, and D_{52}) at different pH values. (B) Isoelectric points of BSA and BSA-GMA with different degrees of methacrylation. (C) Bright-field images of square hydrogel microstructures at different pH values. Scale bar: 5 μm. (D) Effect of different concentrations on the degree of swelling of BSA-GMA hydrogels. (E) Effect of different methylation levels on the degree of swelling of BSA-GMA hydrogels. (F) pH response mechanism of BSA-GMA hydrogels.

in two hydroxyl groups. The isoelectric points of BSA, D_{15}, D_{35}, and D_{52} were not significantly different at 4.62, 4.74, 4.79, and 4.85, respectively. Thus, the modified BSA-GMA still maintained the pH-responsive properties of BSA, while the degree of swelling of the microscopic square structure was adjusted by varying the concentration and the degree of methacrylation of BSA-GMA (Figure 6C). The degree of swelling was slightly higher for the highly concentrated BSA-GMA polymerized cube $R_{40}D_{52}$ compared to $R_{20}D_{52}$. For BSA-GMA with different methacrylic acid degrees, the lower the methacrylic acid degree, the greater the swelling. Consequently, the effect of methacrylic acid degree on swelling was greater than that on concentration. The pH responsiveness of the microstructure was determined by its swelling percentage. The response trends of BSA-GMA hydrogels with different concentrations and methacrylation levels were the same for different pH solutions. Those at pH 2 and pH 11 showed a large swelling, and pH 5 was the inflection point for the swelling of BSA-GMA with the smallest swelling (Figure 6D and E). The swelling rates of $R_{20}D_{52}$, $R_{30}D_{52}$, $R_{40}D_{52}$, $R_{40}D_{35}$, and $R_{40}D_{15}$ increased from 2.41%, 4.16%, 5.28%, 13.25%, and 20.12% for pH 5 solution to 11.96%, 28.38%, 40.67%, 78.78%, and 95.08% for pH 11 solution, respectively. Figure 6F shows the pH response mechanism of BSA-GMA. The isoelectric point of BSA-GMA with different degrees of methacrylation was all in the range of 4.7 to 4.9, so the surface of BSA-GMA is not charged at pH = 5. At pH > 5, the ionization of aspartic acid and glutamic acid makes the surface of BSA-GMA negatively charged. At pH < 5, the protonation of arginine, histidine, and lysine makes the surface positively charged. The swelling of the hydrogel is due to the repulsive force generated by the electrostatic interaction between the amino acids in BSA-GMA. The greater swelling at higher concentrations may be attributed to the greater repulsive force arising from the higher number of negatively charged carboxyl groups or positively charged amino groups in the BSA-GMA microstructure. The higher degree of methacrylation resulted in a greater crosslink density for BSA-GMA photo-crosslinking, which hindered the swelling of the BSA-GMA microstructure. BSA-GMA retains the pH-responsive properties of BSA, and the degree of pH swelling can be adjusted by the degree of methacrylic acidity. The greatest degree of swelling was observed for $R_{40}D_{15}$ at high concentration and low methacrylation degree.

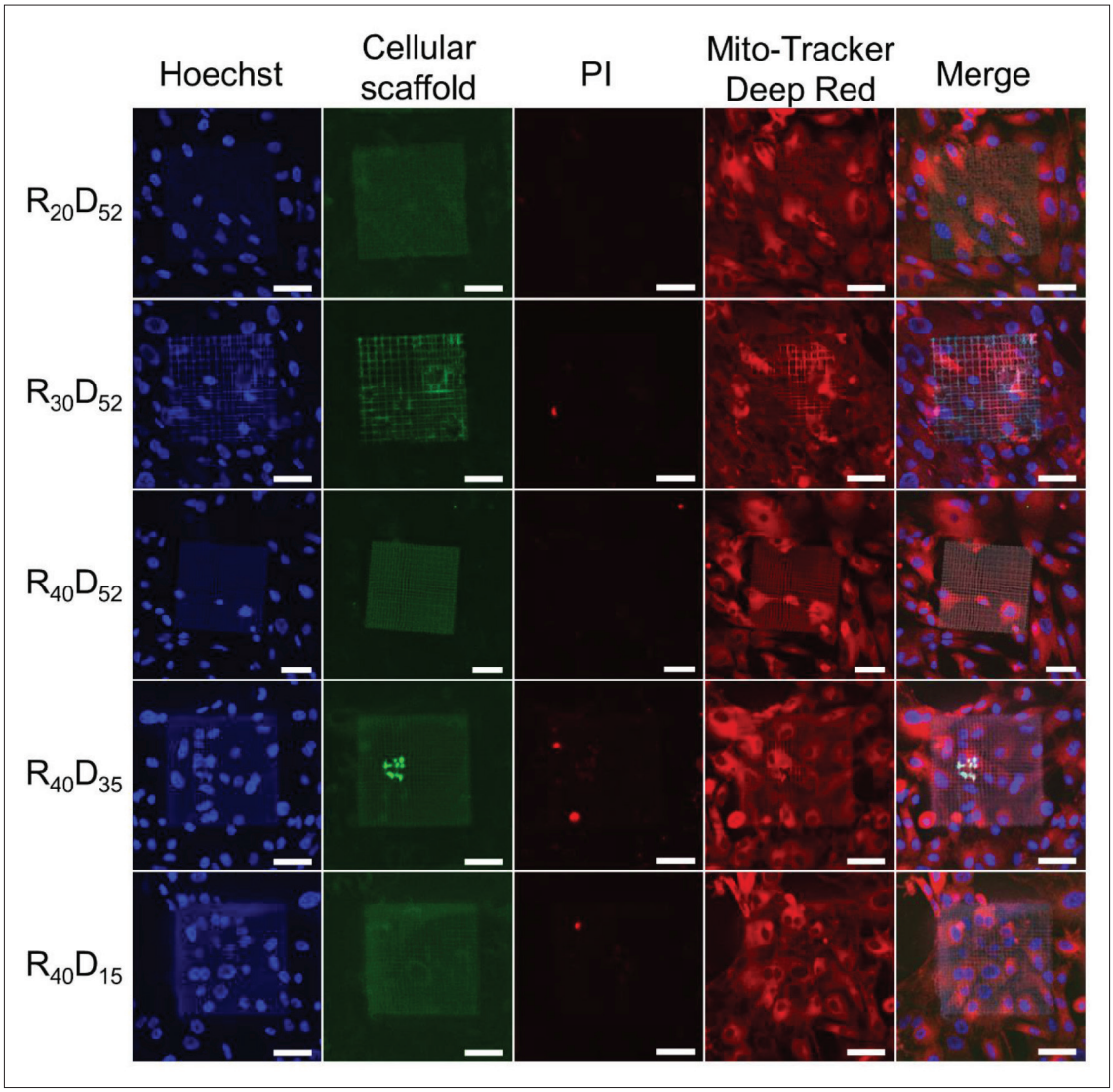

Figure 7. Confocal fluorescence microscopy images of chondrocytes on five hydrogel scaffolds ($R_{20}D_{52}$, $R_{30}D_{52}$, $R_{40}D_{52}$, $R_{40}D_{35}$, and $R_{40}D_{15}$). The excitation wavelengths for the nuclei (Hoechst), cellular scaffold, dead cells (PI), and mitochondria (Mito-Tracker Deep Red) were 405, 488, 561, and 640 nm, respectively. Scale bar: 50 μm.

BSA-GMA hydrogels can also be used as cell scaffolds, and the biocompatibility of the scaffolds is important. Therefore, cell scaffolds with 150 μm^2 woodpile structure were prepared with precursor solutions of $R_{20}D_{52}$, $R_{30}D_{52}$, $R_{40}D_{52}$, $R_{40}D_{35}$, and $R_{40}D_{15}$. Chondrocytes were cultured on these five scaffolds *in vitro* for 3 days. Cell cytotoxicity analysis was used to differentiate between living and dead cells. The nuclei of dead cells were stained with PI (λ_{ex} = 561 nm), while the nuclei and mitochondria of living cells were stained with Hoechst (λ_{ex} = 405 nm) and Mito-Tracker Deep Red (λ_{ex} = 640 nm). The confocal fluorescence images show that chondrocytes were evenly distributed and maintained high cell viability in the five hydrogels (Figure 7). The confocal fluorescence microscopy of each laser channel showed a small number of dead cells and a uniform distribution of living cells.

The 3D images and 3D optical sections of living/dead cells also visually show that the cells are evenly distributed and well spread on the scaffold (Figure 8). The distribution of living and dead cells on each scaffold can be seen in the 3D optical sections of each single channel (**Figure S4** in Supplementary File). There was no significant difference in the proliferation of chondrocytes, good chondrocyte adhesion, and low numbers of dead cells in all five different hydrogels, indicating that BSA-GMA hydrogel has good cytocompatibility for chondrocytes. These results suggest that BSA-GMA as a biocompatible hydrogel is well-suited

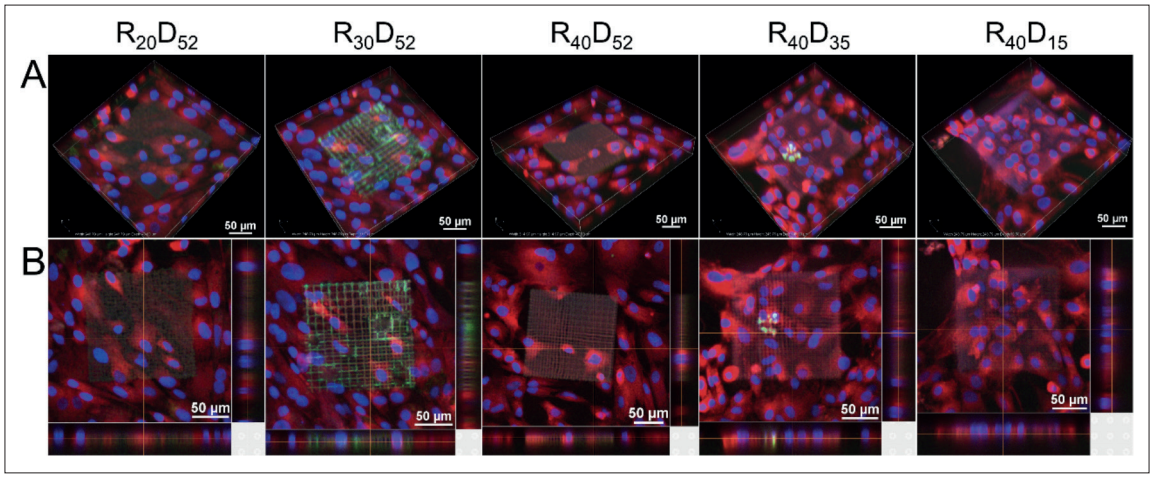

Figure 8. 3D images of confocal fluorescence microscopy of the stained chondrocytes on five hydrogel scaffolds ($R_{20}D_{52}$, $R_{30}D_{52}$, $R_{40}D_{52}$, $R_{40}D_{35}$, and $R_{40}D_{15}$). (A) 3D images of confocal fluorescence microscopy of living/dead stained chondrocytes on five hydrogel scaffolds. (B) Overlay of the 3D optical section of living cells stained by Hoechst, PI, and Mito-Tracker Deep Red on five hydrogel scaffolds.

for the 3D culture of living cells and could be used as a cellular scaffold for subsequent cartilage repair studies.

4. Conclusion

In summary, we demonstrate that GMA-modified BSA (BSA-GMA) can enable the TPP of BSA-GMA in the aqueous phase with the radical type I photoinitiator of LAP. The as-prepared BSA-GMA reduces the consumption of a large number of amino acids during TPP compared to pure BSA. The TPP capability can be regulated by adjusting the degree of methacrylation and concentration. The 3D BSA-GMA hydrogel structures with fine configuration, autofluorescence, pH response, and biocompatibility have been fabricated by femtosecond laser direct writing technique. The chondrocytes attach and grow well on the scaffold since the surface of BSA is negatively charged and similar to the cartilage growth environment in a physiological environment (pH 7.4). Benefiting from the unique optical property and biocompatibility, BSA-GMA hydrogels have good prospects for various biomedical applications. Subsequent research will be directed toward the application of BSA-GMA hydrogels for drug release and cartilage repair.

Acknowledgments

The authors thank the financial support of the International Partnership Program of Chinese Academy of Sciences (GJHZ2021130), National Natural Science Foundation of China (NSFC, Grant Nos. 61975213, 51901234, and 61475164), the National Key R&D Program of China (Grant Nos. 2017YFB1104300 and 2016YFA0200500), and Cooperative R&D Projects between FFG of Austria and CAS of China (GJHZ1720).

The authors also thank Dr. Ye Tian and Prof. Xian-Wei Meng for the discussion about Zeta potential characterization.

Funding

This work was financially supported by the International Partnership Program of Chinese Academy of Sciences (GJHZ2021130), National Natural Science Foundation of China (NSFC, Grant Nos. 61975213, 51901234, and 61475164), the National Key R&D Program of China (Grant Nos. 2017YFB1104300 and 2016YFA0200500), and Cooperative R&D Projects between FFG of Austria and CAS of China (GJHZ1720).

Conflict of interest

The authors declare no conflict of interest.

Author contributions

Conceptualization: Teng Li, Mei-Ling Zheng
Data curation: Jie Liu, Mei-Ling Zheng
Formal analysis: Teng Li, Min Guo, Fan-Chun Bin, Atsushi Nakayama
Investigation: Teng Li, Jie Liu, Wei-Cai Zhang, Jian-Yu Wang, Mei-Ling Zheng
Methodology: Teng Li, Katsumasa Fujita, Mei-Ling Zheng
Project administration: Katsumasa Fujita, Mei-Ling Zheng
Software: Feng Jin, Xian-Zi Dong
Supervision: Mei-Ling Zheng
Validation: Feng Jin, Xian-Zi Dong
Visualization: Jie Liu
Writing – original draft: Teng Li
Writing – review & editing: Mei-Ling Zheng

Ethics approval and consent to participate

Not applicable.

Consent for publication

Not applicable.

Availability of data

The data can be obtained from the authors.

References

1. Tang H, Bi F, Chen G, *et al.*, 2022, 3D-bioprinted recombination structure of Hertwig's epithelial root sheath cells and dental papilla cells for alveolar bone regeneration. *Int J Bioprint*, 8(3): 140–150.

   https://doi.org/10.18063/ijb.v8i3.512

2. Anandakrishnan N, Ye H, Guo Z, *et al.*, 2021, Fast stereolithography printing of large-scale biocompatible hydrogel models. *Adv Healthc Mater*, 10(10): 2002103.

   https://doi.org/10.1002/adhm.202002103

3. Liu X, Chen M, Luo J, *et al.*, 2021, Immunopolarization-regulated 3D printed-electrospun fibrous scaffolds for bone regeneration. *Biomaterials*, 276: 121037.

   https://doi.org/10.1016/j.biomaterials.2021.121037

4. Wang Z, Wang Y, Yan J, *et al.*, 2021, Pharmaceutical electrospinning and 3D printing scaffold design for bone regeneration. *Adv Drug Deliv Rev*, 174: 504–534.

   https://doi.org/10.1016/j.addr.2021.05.007

5. Melchels FPW, Feijen J, Grijpma DW, 2010, A review on stereolithography and its applications in biomedical engineering. *Biomaterials*, 31(24): 6121–6130.

   https://doi.org/10.1016/j.biomaterials.2010.04.050

6. Gou X, Guo Z, 2021, Reed leaf-inspired anisotropic slippery lubricant-infused surface for water collection and bubble transportation. *J Chem Eng*, 411: 128495.

   https://doi.org/10.1016/j.cej.2021.128495

7. Primo GA, Mata A, 2021, 3D patterning within hydrogels for the recreation of functional biological environments. *Adv Funct Mater*, 31(16): 2009574.

   https://doi.org/10.1002/adfm.202009574

8. Zhang J, Hu Q, Wang S, *et al.*, 2020, Digital light processing based three-dimensional printing for medical applications. *Int J Bioprint*, 6(1):12–27.

   https://doi.org/10.18063/ijb.v6i1.242

9. Zhao J, Cui W, 2020, Functional electrospun fibers for local therapy of cancer. *Adv Fiber Mater*, 2(5): 229–245.

   https://doi.org/10.1007/s42765-020-00053-9

10. Li Y, Shen Q, Shen J, *et al.*, 2021, Multifunctional fibroblasts enhanced via thermal and freeze-drying post-treatments of aligned electrospun nanofiber membranes. *Adv Fiber Mater*, 3(1): 26–37.

    https://doi.org/10.1007/s42765-020-00059-3

11. Murphy C, Kolan K, Li WB, *et al.*, 2017, 3D bioprinting of stem cells and polymer/bioactive glass composite scaffolds for bone tissue engineering. *Int J Bioprint*, 3(1): 54–64.

    https://doi.org/10.18063/ijb.2017.01.005

12. Lan X, Liang Y, Vyhlidal M, *et al.*, 2022, In vitro maturation and in vivo stability of bioprinted human nasal cartilage. *J Tissue Eng*, 13: 20417314221086368.

    https://doi.org/10.1177/20417314221086368

13. Jin F, Liu J, Zhao Y-Y, *et al.*, 2022, Lambda/30 inorganic features achieved by multi-photon 3D lithography. *Nat Commun*, 13(1):1357.

    https://doi.org/10.1038/s41467-022-29036-7

14. Sun Y-L, Dong W-F, Niu L-G, *et al.*, 2014, Protein-based soft micro-optics fabricated by femtosecond laser direct writing. Light Sci Appl, 3(1): e129.

    https://doi.org/10.1038/lsa.2014.10

15. Kumi G, Yanez CO, Belfield KD, *et al.*, 2010, High-speed multiphoton absorption polymerization: Fabrication of microfluidic channels with arbitrary cross-sections and high aspect ratios. *Lab Chip*, 10(8): 1057–1060.

    https://doi.org/10.1039/b923377f

16. Bin FC, Guo M, Li T, *et al.*, 2023, Carbazole-based anion ionic water-soluble two-photon initiator for achieving 3D hydrogel structures. *Adv Funct Mater,* 2300293.

    https://doi.org/10.1002/adfm.202300293

17. Kufelt O, El-Tamer A, Sehring C, *et al.*, 2015, Water-soluble photopolymerizable chitosan hydrogels for biofabrication via two-photon polymerization. *Acta Biomater*, 18: 186–195.

    https://doi.org/10.1016/j.actbio.2015.02.025

18. Paun IA, Mustaciosu CC, Popescu RC, *et al.*, 2020, Collagen/chitosan functionalization of complex 3D structures fabricated by laser direct writing via two-photon polymerization for enhanced osteogenesis. *Int J Mol Sci*, 21(17): 6246–6264.

    https://doi.org/10.3390/ijms21176426

19. Xing J-F, Zheng M-L, Duan X-M, 2015, Two-photon polymerization microfabrication of hydrogels: An advanced 3D printing technology for tissue engineering and drug delivery. *Chem Soc Rev*, 44(15): 5031–5039.

    https://doi.org/10.1039/c5cs00278h

20. Bozuyuk U, Yasa O, Yasa IC, *et al.*, 2018, Light-triggered drug release from 3D-printed magnetic chitosan microswimmers. *ACS Nano*, 12(9): 9617–9625.

    https://doi.org/10.1021/acsnano.8b05997

21. Zhang YS, Khademhosseini A, 2017, Advances in engineering hydrogels. *Science*, 356(6337): 124875.

https://doi.org/10.1126/science.aaf3627

22. Armiento AR, Stoddart MJ, Alini M, *et al.*, 2018, Biomaterials for articular cartilage tissue engineering: Learning from biology. *Acta Biomater*, 65: 1–20.

https://doi.org/10.1016/j.actbio.2017.11.021

23. Hu C, Long L, Cao J, *et al.*, 2021, Dual-crosslinked mussel-inspired smart hydrogels with enhanced antibacterial and angiogenic properties for chronic infected diabetic wound treatment via pH-responsive quick cargo release. *J Chem Eng*, 411: 128564.

https://doi.org/10.1016/j.cej.2021.128564

24. Yang Z, Huang R, Zheng B, *et al.*, 2021, Highly stretchable, adhesive, biocompatible, and antibacterial hydrogel dressings for wound healing. *Adv Sci*, 8(8): 2003627.

https://doi.org/10.1002/advs.202003627

25. Wang J-Y, Jin F, Dong X-Z, *et al.*, 2022, Flytrap inspired pH-driven 3D hydrogel actuator by femtosecond laser microfabrication. *Adv Mater Technol*, 7(8): 2200276.

https://doi.org/10.1002/admt.202200276

26. Lee A, Hudson AR, Shiwarski DJ, *et al.*, 2019, 3D bioprinting of collagen to rebuild components of the human heart. *Science*, 365(6452): 482–487.

https://doi.org/10.1126/science.aav9051

27. Yang J, Xiao Y, Tang Z, *et al.*, 2020, The negatively charged microenvironment of collagen hydrogels regulates the chondrogenic differentiation of bone marrow mesenchymal stem cells in vitro and in vivo. *J Mater Chem B*, 8(21): 4680–4693.

https://doi.org/10.1039/d0tb00172d

28. Hu C, Lu W, Mata A, *et al.*, 2021, Ions-induced gelation of alginate: Mechanisms and applications. *Int J Biol Macromol*, 177: 578–588.

https://doi.org/10.1016/j.ijbiomac.2021.02.086

29. Wang L, Zhang X, Yang K, *et al.*, 2020, A novel double-crosslinking-double-network design for injectable hydrogels with enhanced tissue adhesion and antibacterial capability for wound treatment. *Adv Funct Mater*, 30(1): 1904156.

https://doi.org/10.1002/adfm.201904156

30. Shin J, Lee JS, Lee C, *et al.*, 2015, Tissue adhesive catechol-modified hyaluronic acid hydrogel for effective, minimally invasive cell therapy. *Adv Funct Mater*, 25(25): 3814–3824.

https://doi.org/10.1002/adfm.201500006

31. Yu H, Liu J, Zhao Y-Y, *et al.*, 2019, Biocompatible three-dimensional hydrogel cell scaffold fabricated by sodium hyaluronate and chitosan assisted two-photon polymerization. *ACS Appl Bio Mater*, 2(7): 3077–3083.

https://doi.org/10.1021/acsabm.9b00384

32. Zhang W-C, Zheng M-L, Liu J, *et al.*, 2021, Modulation of cell behavior by 3D biocompatible hydrogel microscaffolds with precise configuration. *Nanomaterials*, 11(9): 2325.

https://doi.org/10.3390/nano11092325

33. Zhang Q, Liu Y, Yang G, *et al.*, 2023, Recent advances in protein hydrogels: From design, structural and functional regulations to healthcare applications. *J Chem Eng*, 451: 138494.

https://doi.org/10.1016/j.cej.2022.138494

34. Baler K, Michael R, Szleifer I, *et al.*, 2014, Albumin hydrogels formed by electrostatically triggered self-assembly and their drug delivery capability. *Biomacromolecules*, 15(10): 3625–3633.

https://doi.org/10.1021/bm500883h

35. Giang Phan VH, Thambi T, Kim BS, *et al.*, 2017, Engineering highly swellable dual-responsive protein-based injectable hydrogels: The effects of molecular structure and composition in vivo. *Biomater Sci*, 5(11): 2285–2294.

https://doi.org/10.1039/c7bm00707h

36. Sabaa MW, Hanna DH, Abu Elella MH, *et al.*, 2019, Encapsulation of bovine serum albumin within novel xanthan gum based hydrogel for protein delivery. *Mater Sci Eng C*, 94: 1044–1055.

https://doi.org/10.1016/j.msec.2018.10.040

37. Upadhyay A, Kandi R, Rao CP, 2018, Injectable, self-healing, and stress sustainable hydrogel of BSA as a functional biocompatible material for controlled drug delivery in cancer cells. *ACS Sustain Chem Eng*, 6(3): 3321–3330.

https://doi.org/10.1021/acssuschemeng.7b03485

38. Khoury LR, Popa I, 2019, Chemical unfolding of protein domains induces shape change in programmed protein hydrogels. *Nat Commun*, 10: 5439.

https://doi.org/10.1038/s41467-019-13312-0

39. Cheng L, Cai Z, Ye T, *et al.*, 2020, Injectable polypeptide-protein hydrogels for promoting infected wound healing. *Adv Funct Mater*, 30(25): 2001196.

https://doi.org/10.1002/adfm.202001196

40. Liu W, Sun J, Sun Y, *et al.*, 2020, Multifunctional injectable protein -based hydrogel for bone regeneration. *J Chem Eng*, 394: 124875.

https://doi.org/10.1016/j.cej.2020.124875

41. Yuan H, Zheng X, Liu W, *et al.*, 2020, A novel bovine serum albumin and sodium alginate hydrogel scaffold doped

with hydroxyapatite nanowires for cartilage defects repair. *Colloids Surf B*, 192: 111041.

https://doi.org/10.1016/j.colsurfb.2020.111041

42. Lyu S-R, Kuo Y-C, Lin M-H, *et al.*, 2012, Application of albumin-grafted scaffolds to promote neocartilage formation. *Colloids Surf B*, 91: 296–301.

https://doi.org/10.1016/j.colsurfb.2011.11.019

43. Amdursky N, Mazo MM, Thomas MR, *et al.*, 2018, Elastic serum-albumin based hydrogels: Mechanism of formation and application in cardiac tissue engineering. *J Mater Chem B*, 6(35): 5604–5612.

https://doi.org/10.1039/c8tb01014e

44. Fu F, Chen Z, Zhao Z, *et al.*, 2017, Bio-inspired self-healing structural color hydrogel. *Proc Natl Acad Sci USA*, 114(23): 5900–5905.

https://doi.org/10.1073/pnas.1703616114

45. Kaehr B, Shear JB, 2008, Multiphoton fabrication of chemically responsive protein hydrogels for microactuation. *Proc Natl Acad Sci USA*, 105(26): 8850–8854.

https://doi.org/10.1073/pnas.0709571105

46. Gao W, Chao H, Zheng Y-C, *et al.*, 2021, Ionic carbazole-based water-soluble two-photon photoinitiator and the fabrication of biocompatible 3D hydrogel scaffold. *ACS App Mater Interfaces*, 13(24): 27796–27805.

https://doi.org/10.1021/acsami.1c02227

47. Zheng Y-C, Zhao Y-Y, Zheng M-L, *et al.*, 2019, Cucurbit 7 uril-carbazole two-photon photoinitiators for the fabrication of biocompatible three-dimensional hydrogel scaffolds by laser direct writing in aqueous solutions. *ACS Appl Mater Interfaces*, 11(2): 1782–1789.

https://doi.org/10.1021/acsami.8b15011

48. Xing J, Liu J, Zhang T, *et al.*, 2014, A water soluble initiator prepared through host-guest chemical interaction for microfabrication of 3D hydrogels via two-photon polymerization. *J Mater Chem B*, 2(27): 4318–4323.

https://doi.org/10.1039/c4tb00414k

49. Fairbanks BD, Schwartz MP, Bowman CN, *et al.*, 2009, Photoinitiated polymerization of PEG-diacrylate with lithium phenyl-2,4,6-trimethylbenzoylphosphinate: Polymerization rate and cytocompatibility. *Biomaterials*, 30(35): 6702–6707.

https://doi.org/10.1016/j.biomaterials.2009.08.055

50. Balasubramanian D, Du X, Zigler JS, 1990, The reaction of singlet oxygen with proteins, with special reference to crystallins. *Photochem Photobiol*, 52(4): 761–768.

https://doi.org/10.1111/j.1751-1097.1990.tb08679.x

51. Pitts JD, Campagnola PJ, Epling GA, *et al.*, 2000, Submicron multiphoton free-form fabrication of proteins and polymers: Studies of reaction efficiencies and applications in sustained release. *Macromolecules*, 33(5): 1514–1523.

https://doi.org/10.1021/ma9910437

52. Reis AV, Fajardo AR, Schuquel ITA, *et al.*, 2009, Reaction of glycidyl methacrylate at the hydroxyl and carboxylic groups of poly(vinyl alcohol) and poly(acrylic acid): Is this reaction mechanism still unclear? *J Org Chem*, 74(10): 3750–3757.

https://doi.org/10.1021/jo900033c

53. Kim SH, Yeon YK, Lee JM, *et al.*, 2018, Precisely printable and biocompatible silk fibroin bioink for digital light processing 3D printing. *Nat Commun*, 9(1): 1620.

https://doi.org/10.1038/s41467-018-04517-w

54. Ezerskyte E, Vengris M, Gineitis K, *et al.*, 2022, Qualitative comparison between different biopolymers for usage in two- photon polymerization towards liver regeneration. *Opt Mater Express*, 12(7): 2550–2567.

https://doi.org/10.1364/ome.459057

55. Xu H, Casillas J, Krishnamoorthy S, *et al.*, 2020, Effects of Irgacure 2959 and lithium phenyl-2,4,6-trimethylbenzoylphosphinate on cell viability, physical properties, and microstructure in 3D bioprinting of vascular-like constructs. *Biomed Mater*, 15(5): 055021.

https://doi.org/10.1088/1748-605X/ab954e

56. Lantigua D, Nguyen MA, Wu X, *et al.*, 2020, Synthesis and characterization of photocrosslinkable albumin-based hydrogels for biomedical applications. *Soft Matter*, 16(40): 9242–9252.

https://doi.org/10.1039/d0sm00977f

57. Yu H, Ding H, Zhang Q, *et al.*, 2021, Three-dimensional direct laser writing of PEGda hydrogel microstructures with low threshold power using a green laser beam. *Light: Adv Manuf*, 2(1): 31–38.

https://doi.org/10.37188/lam.2021.003

58. Mueller JB, Fischer J, Mayer F, *et al.*, 2014, Polymerization kinetics in three-dimensional direct laser writing. *Adv Mater*, 26(38): 6566–6571.

https://doi.org/10.1002/adma.201402366

59. Klotz BJ, Gawlitta D, Rosenberg AJWP, *et al.*, 2016, Gelatin-methacryloyl hydrogels: Towards biofabrication-based tissue repair. *Trends Biotechnol*, 34(5): 394–407.

https://doi.org/10.1016/j.tibtech.2016.01.002

60. Al-Shamiri HAS, Abou Kana MTH, Azzouz IM, *et al.*, 2009, Photo-physical properties and quantum yield of some laser dyes in new polymer host. *Opt Laser Technol*, 41(4): 415–418.

https://doi.org/10.1016/j.optlastec.2008.08.008

61. Sandner B, Kammer S, Wartewig S, 1996, Crosslinking copolymerization of epoxy methacrylates as studied by

Fourier transform Raman spectroscopy. *Polymer*, 37(21): 4705–4712.

https://doi.org/10.1016/s0032-3861(96)00325-4

62. Ma X, Sun X, Hargrove D, *et al.*, 2016, A biocompatible and biodegradable protein hydrogel with green and red autofluorescence: Preparation, characterization and in vivo biodegradation tracking and modeling. *Sci Rep*, 6(1): 19370.

https://doi.org/10.1038/srep19370

63. Wei S, Liu J, Zhao Y, *et al.*, 2017, Protein-based 3D microstructures with controllable morphology and pH-responsive properties. *ACS Appl Mater Interfaces*, 9(48): 42247–42257.

https://doi.org/10.1021/acsami.7b14915

64. Lay CL, Lee MR, Lee HK, *et al.*, 2015, Transformative two-dimensional array configurations by geometrical shape-shifting protein microstructures. *ACS Nano*, 9(10): 9708–9717.

https://doi.org/10.1021/acsnano.5b04300

65. Ma Z-C, Zhang Y-L, Han B, *et al.*, 2020, Femtosecond laser programmed artificial musculoskeletal systems. *Nat Commun*, 11(1): 4536.

https://doi.org/10.1038/s41467-020-18117-0